Structural Analysis for Tensile Behavior of Silicon-Carbon Core-Shell Nanotube

Structural Analysis for Tensile Behavior of Silicon-Carbon Core-Shell Nanotube

Min Li[1,a], Zean Tian[2,b], Quan Xie[3,c*], Kejun Dong[4,d]

[1]College of big data and information engineering Guizhou University Guiyang, China

[2]College of big data and information engineering Guizhou University Guiyang, China

[3]College of big data and information engineering Guizhou University Guiyang, China

[4]Center for Infrastructure Engineering, School of Computing, Engineering and Mathematics Western Sydney University Penrith, NSW, Australia

[a]e-mail: minli_gzcn@sina.com, [b]e-mail: tianzean@126.com

[c*]Corresponding Author e-mail: qxie@gzu.edu.cn

[d]e-mail: Kejun.dong@westernsydney.edu.au

Abstract: This paper presents a molecular dynamics study on the tensile behavior of carbon nanotubes (CNT) with or without nanowire of Si (SiNW) encapsulated. Compared to the CNT without SiNW, the CNT with the SiNW (denoted as SiNW@CNT) shows a decreased tensile strength but an increased maximum tensile deformation rate. The micromechanisms of the different tensile behaviors were explored through the structural analysis including the radial distribution function, the bond angle distribution function, and the statistics of the polygon defects. The results showed that the C-C bond in the CNT under the maximum tensile deformation becomes longer and more uniform due to the van der Waals force between the SiNW and the CNT, which accounts for the change in the macroscopical tensile behavior. Moreover, it has been found that after tensile fracture, the CNT mainly form long chains consisting of triangle, pentagon, and heptagonal defects, while SiNW@CNT cannot form long chains due to the lack of triangular defects. These differences in the microstructures are probably because the C-C bonds in the SiNW@CNT can be strengthened by the SiNW. The results provide a better understanding of the fracture of the CNT and its nano composites, and have certain reference value for the application of the SiNW@CNT.

1. INTRODUCTION

Carbon nanotubes (CNT), one of the strongest and hardest materials in terms of tensile strength and modulus of elasticity, have received widespread attention since they were discovered by Iijima in 1991 [1]. CNTs were used to develop superconducting devices due to their extraordinary electrical, thermal, mechanical [2, 3] and other excellent properties. The unique and elegant hollow structure of the CNT enables the introduction of "exotic" materials such as metal, carbides, oxides, or even proteins, which can result in “CNT composites” with greatly improved electronic, catalytic or mechanical properties [4]. Compared to traditional materials, high-performance composites [5] are stronger, lighter, or cheaper, and are becoming more and more indispensable in many fields.

The tensile properties of CNTs were found to possess excellent features from theoretical, experimental and numerical studies [6]. For CNT nanocomposites with encapsulated component, the tensile properties

may be affected. Wang et al. studied the axial buckling of the single-walled CNT filled with metal atoms and found that the critical buckling strain can increase as the encapsulated atoms increase [7]. T.Belytschko et al. conducted molecular dynamics (MD) study on the fracture of the single-walled CNT from the perspective of energy [8]. Similarly, it was found that the CNT can also be used to protect the silicon nanowire (SiNW), because the carbon layers can not only effectively separate the oxygen and Si atoms to reduce the oxidation of Si, but also neutralize the unsaturated bonds on the surface of the inner SiNW [9]. At the same time, the SiNW can enhance the mechanical properties of the CNT. Therefore, the composite structure composed of a SiNW and the covering CNT (SiNW@CNT) may have more abundant physical properties and have important application prospects in future micro-nano electronics.

However, due to the limitation of experiments, such as difficulties in tracking the movement of atoms for a long time, comprehensive understanding the microstructure, mechanical properties and intrinsic mechanism of nanomaterials [10] usually needs to utilize the advantages of computer simulation to assist experiment studies. In this paper, MD simulation is applied to investigate the tensile behavior of the CNT and SiNW@CNT. The radial distribution function and the bond angle distribution function were used to analyze the micro-mechanisms of the macrosocial tensile behaviors of the two materials. Furthermore, a quantitative statistic of the numbers of different polygon defects were performed to reveal the variations of the topological proprieties of the lattices in the final stage. These results provide a clearer picture for the lattice deformation during tensile fracture for the two materials, which can improve the understanding of the fracture of the CNT and its nano-composites and have certain reference value for the potential application of the SiNW@CNT.

2. METHODOLOGY

2.1. Simulation details

The mechanical properties of a SiNW with a certain diameter filled in armchair CNT (15,15) were studied by MD simulation, and this SiNW is intercepted from bulk silicon along the crystal direction [111]; For convenience, this kind of composite structure is briefly described as [hkl]@ (n,n), and it is [111]@(15,15) for the composite mentioned above. The armchair CNT is 2.034 nm in diameter, 11.5597 nm in length. There are 2,820 atoms in CNT and 469 atoms in the SiNW.

A key point in MD simulation is the selection of potential function. In this study, the Tersoff potential [11] was adopted to model C-C in the CNT and Si-Si in the SiNW. The average distance between the outer atoms of the SiNW and the CNT wall is about 5.78 Å , and thus the interaction between them is the long-range van der Waals potential using the Lennard–Jones potential [12], which is defined as follows:

$$V_{LJ}(r) = 4\varepsilon\left[\frac{\sigma^{12}}{r} - \frac{\sigma^{6}}{r}\right], \quad r < r_{\text{cutoff}} \tag{1}$$

where the energy parameter ε = 8.399 meV, the distance parameter σ = 3.326 Å, and r is the interatomic distance; r_{cutoff} is the cut-off distance, which is set as 8.315 Å. These parameters are based on the van der Waals interaction in the universal force field model [13].

The system was first relaxed isothermally for 5 ps at 300 K under NPT to get the minimum energy structure, and the time step was 0.5 fs. Free boundary conditions were adopted in all three directions. In order to reduce the thermal influence [14], the temperature was controlled by the Berendsen thermostat [15] around 1 K during the stretching simulation. The atoms within four layers at each end of the CNT were fixed and the axial displacement was applied in a rate of 0.04 Å per 1000 steps, lasting for 1.5 ns. Figure 1(a) and Figure 1(b) show the front and top of [111]@(15,15) respectively. And Figures 1(c) and 1(d) are the snapshots at the tensile deformation rate of 36.92% and 36.96%, respectively.

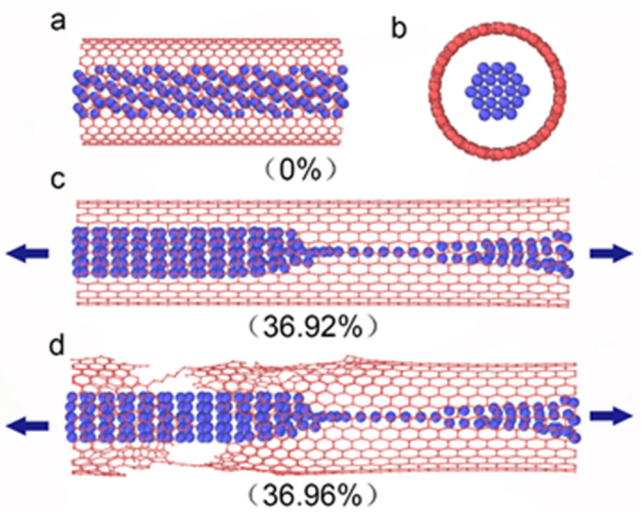

Figure 1. The 3D views of the simulated SiNW@CNT [111]@(15,15) with the free boundary conditions in all three dimensions. Front view (a), and top view (b) at the initial state. Simulation snapshots at strain 36.92% (c) and 36.96% (d).

2.2. Structural analysis methods

Three methods were employed to identify the microstructure characteristics of the CNT and the SiNW@CNT in the tensile deformation. They can reveal the detailed changes of the bond length, bond angle and polygon defects of the two materials.

The first one is the radial distribution function [16] (RDF), which is not only a statistical parameter about the distances between atoms in a system, but also an important structural parameter verifying the results of a simulation. Because it can be obtained by a Fourier transform of the structural factors that can be measured by X-ray diffraction experiments. The RDF is defined as:

$$\mathrm{g(r)} = \frac{n(r)}{3} 4\pi\rho r^2 \Delta r = \frac{V}{N(N-1)} \sum_{i=1}^{N} \sum_{j\neq 1}^{N} \delta(r - r_{ij}), \quad (2)$$

where N is the total number of atoms in a system. The value of g(r) denotes the average probability of finding other particles in a unit volume at a distance r from a reference atom.

The second one is the Angular Distribution Function [17] (ADF), which describes the statistics of the angles formed by any pair of neighboring atoms with respect to the center atom, defined as:

$$\mathrm{X}(\cos\theta, \mathrm{r}) = \frac{n(\cos\theta, r)}{N(\theta, r)} = \frac{1}{N(\theta, r)} \sum_{i=1}^{N} \sum_{j\neq i}^{r_{ij}<r} \sum_{k\neq i}^{r_{ik}<r} \delta\left(\cos\theta - \frac{r_{ij} r_{ik}}{|r_{ij}||r_{ik}|}\right), \quad (3)$$

where $N(\theta, r)$ is the normalization factor and represents all the number of calculated angles composed of any two neighbors together with the center of an atom, and our calculation covers all atoms in the system.

The third one is the statistics of the polygon defects. In the literature, it was found that during the tensile deformation, some hexagonal lattices in the CNT will become polygons with edge numbers different from 6. These polygon defects were normally only analyzed through visualization. Here we present quantitative statistics for the numbers of different polygon defects. The method requires a pre-set constant cut-off distance r_c to determine the bonded atoms. Here it was set as the value of the first wave trough of the RDF. Then the closed polygons and the edge numbers of them were counted. The numbers of defected polygons with different edges were analyzed.

3. Results and Discussions

3.1. Stress-strain relation

The stress-strain relationship of a material during tensile deformation can reflect its basic mechanical properties. As shown in Figure 2, the tensile processes of the CNT(15,15) and SiNW@CNT(15,15) were

both similar to that of metals [18], going through four stages: linear elastic deformation, yield deformation, strengthening stage and local deformation. Although the stress and strain values have changed to a certain extent in 1 K in Figure 2(a) and 300 K in Figure 2(b), the positive proportional relationship between CNT and SiNW@CNT has not changed, and the trend of each stage at 1 K tensile is more obvious and less affected by thermal vibration, so the stress-strain relationship at 1K is mainly discussed in this article.

For the CNT (15,15) and SiNW@CNT (15,15) at 1 K in Figure 2(a), the simulated maximal effective strains were 0.34 and 0.41 respectively. The linear elastic deformation stage should be linked to the linear increase of the stress with the small strain, which was from $\varepsilon = -0.024$ to $\varepsilon = 0.027$ for the CNT and $\varepsilon = 0.016$ to $\varepsilon = 0.047$ for the SiNW@CNT. However, the strengthening stage (also known as strain hardening) was very obvious, and the material strength was further improved with the stain further increased beyond this point. This stage was from $\varepsilon = 0.238$ to $\varepsilon = 0.340$ for the CNT and $\varepsilon = 0.260$ to $\varepsilon = 0.412$ for the SiNW@CNT. The local deformation stage was very short. As found in the literature, with the continuous stretching of the carbon tube, stone-wales defects [19] will appear in the radial direction, and the C-C bonds will begin to break and reorganize. Here they were manifested by a sharp shrinkage of the tube diameter and the emergence of the necking phenomenon [20], which causes the stress to reduce suddenly.

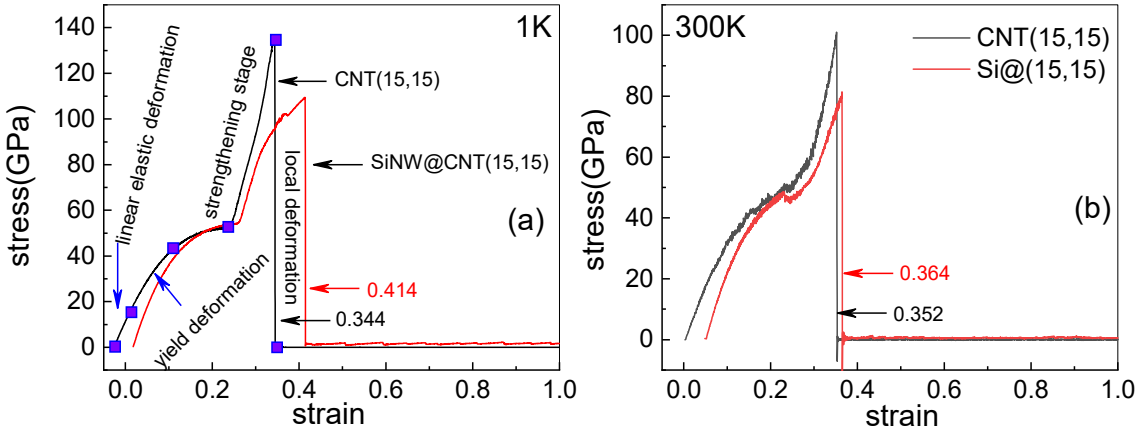

Figure 2. The strain-stress curve of CNT (15,15) and SiNW@CNT (15,15) at 1 K for (a) and 300 K for (b).

As can be seen from Figure 2(a), the simulated maximum strain (tensile deformation rate) of SiNW@CNT was 41.2%, higher than that of the CNT at 34.4%; but the simulated maximum stress (tensile strength) of SiNW@CNT was 109.05 GPa, lower than that of the CNT (134.62 GPa). Although the stress of the SiNW@CNT is shared by the CNT and the SiNW, the yield of the SiNW during the strengthening stage results in the overall increase of the strain but the decrease of the stress. It is noteworthy that the non-zero strain at zero strain (see the left bottom corner of Figure 2(a)) results from the relaxation process during which the length of the CNT shrinked slightly, while that of SiNW@CNT elongated slightly. Also note that the simulated maximum strain 34.4% for the CNT is closer to the measured value of 30% for faultless CNT [21] but much higher than 21% measured in the CNT with a small number of impurities [22]. This shows that our simulation result is in reasonable agreement with the measured value and the strength of the CNT can be significantly affected by the impurities.

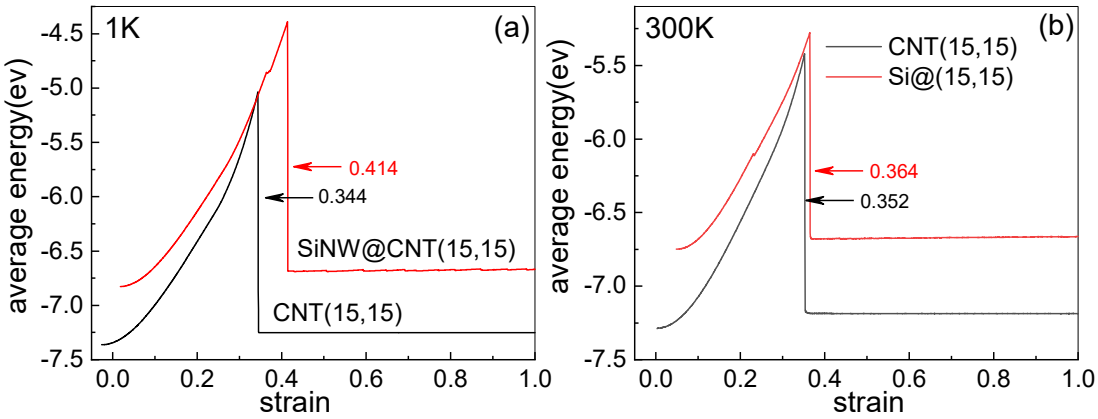

Figure 3. The evolution of the atom average energy of CNT (15,15) and SiNW@CNT (15,15) at 1 K for (a) and 300 K for (b).

However, the evolution of the average energy of the atoms in Figure 3 was much different from that of stress, with only two stages, a linear increase followed by a drop-off. Whether in Figure 3(a) at 1 K or Figure 3(b) at 300 K, the atom average energies of the CNT and SiNW@CNT both increased first to the maximum and then dropped sharply to a constant value at the time of fracture. In particular, the atom average energy of the CNT in Figure 3(a) before the stretching was -7.36 eV, which increased linearly to the maximum value of -5.05 eV, and then decreased vertically to -7.25 eV and remained constant; the corresponding values of the SiNW@CNT were respectively -6.83 eV, -4.41 eV and -6.68 eV. The atom average energy of the SiNW@CNT was always larger than that of the CNT, indicating that the energy of Si atoms is larger than that of C atoms averagely. And the energy curve of the CNT is basically consistent with the results simulated by M.A et al [23].

The specific parameters before and after relaxation about 1 K are shown in Table 1. L_0 and L_1 are the axial lengths before and after relaxation, and Φ_0 and Φ_1 are the diameters before and after relaxation, respectively. Although CNT and SiNW will cause a partial lattice mismatch due to the variation of length and diameter before and after relaxation, it can be seen from the ratio in Table 1 that this mismatch is very small compared to its intermolecular distance and basically will not affect its mechanical properties. It has been confirmed in the literature [24] that the mechanical properties of the CNT are mainly related to its chirality, the slight changes in axial and radial direction will not affect their mechanical properties.

Table 1. The parameters of models before and after relaxation.

Type	Atoms	L_0(Å)	L_1(Å)	$\frac{L_1 - L_0}{L_0}$	Φ_0(Å)	Φ_1(Å)	$\frac{\Phi_1 - \Phi_0}{\Phi_0}$
CNT(15,15)	2820	115.597	114.28	**-1.14**	20.34	20.89	**2.70**
SiNW@CNT (15,15)	3289	115.597	117.565	**1.70**	20.34	21.15	**3.98**
SiNW	469	113.75	116.834	**2.71**	8.79	8.85	**0.68**

3.2. Bond length and bond angle at fracture point

Bond length and bond angle can reflect the microscopic changes of the materials structure during tensile deformation, which can be measured through the RDF [16] and ADF [17]. In order to understand the micro-structure of the CNT and composite CNT in depth and intuitively, the software Ovito [25] was used to visualize them.

The RDF of the CNT and SiNW@CNT were firstly analyzed at the maximum tensile deformation of 34.40% and 41.41% respectively, which are shown in Figure 4, and their snapshots are shown in Figure

6. P1 to P4 are the first, second, third and fourth major peaks in Figure 4(a) respectively, with their positions measured at 1.39 Å, 1.56 Å, 1.74 Å and 1.79 Å respectively. By carefully checking the typical segments shown in Figure 6, it is found that P1 to P4 correspond to the four bonds in different colors in Figure 6(a): P1: red, P2: green, P3: yellow, and P4: blue. Here the red bonds (P1) are the shortest bonds at the end of the tube with almost the same lengths as the non-deformed CNT. The green (P2) bonds are the horizontal C-C bonds that slightly elongated. The yellow (P3) bonds and blue (P4) bonds are those two non-horizontal C-C bonds, which have relatively large deformation. P4 is slightly longer than P3, but their values are rather close. These peaks are all narrow in Figure 4(a), showing that the deformed lattices were rather similar.

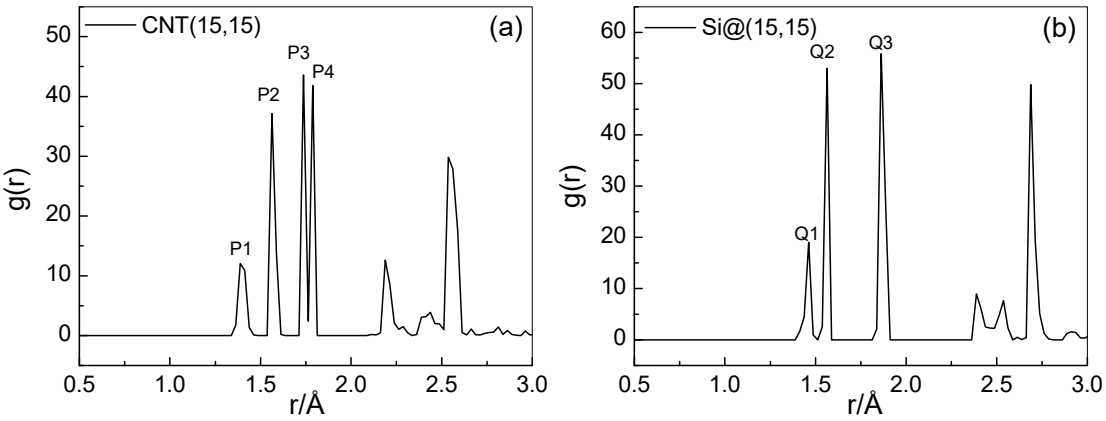

Figure 4. RDF for CNT (15,15) (a) and SiNW@CNT (15,15) (b) at the maximum tensile deformation of 34.40% and 41.41% respectively.

Similarly, as shown in Figure 4(b), Q1-Q3 are the first, second and third major peaks at 1.46 Å, 1.56 Å and 1.86 Å respectively, corresponding to the three bonds in the deformed lattices of the SiNW@CNT. These bonds are in different colors in Figure 6(b): Q1: red, Q2: green and Q3: blue. Compared to the deformed lattices of the CNT, the position of the second peak (Q2 in Figure 6) of the SiNW@CNT was the same (P2 in Figure 6). But the Q3 bond length of the SiNW@CNT was longer than the longest bond length (P4) of the CNT. And the shortest bond Q1 of SiNW@CNT was also longer than that (P1) of the CNT. The comparison shows that the encapsulation of the SiNW in the CNT not only makes the C-C bonds longer, but also makes the deformed bonds along the tensile direction more uniform in length.

From the sharp peaks in Figure 4(a) and (b), it can be seen that in our simulations, the lattices of the CNT and SiNW@CNT both changed uniformly in the process of tensile fracture, which is in accordance with the literature [23]. Only in the fractured CNT, there is a small difference between the two non-horizontal bonds (P3 and P4), which is probably due to a small deformation like buckling along the horizontal direction. Whereas in the SiNW@CNT, such a small difference was eliminated as there are van der Waals forces between the inserted Si atoms and the C atoms at the tube wall, which can depress such deformation.

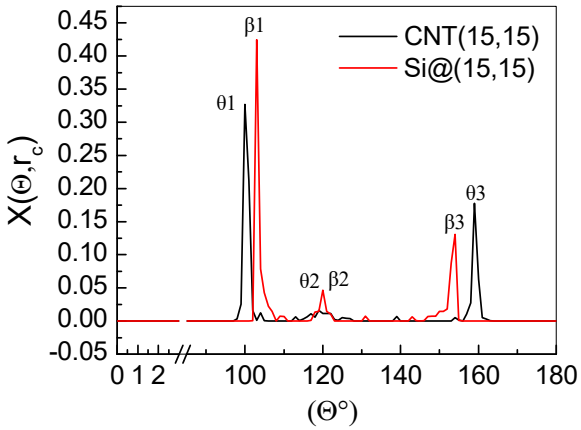

Figure 5. Bond angle distributions of the CNT and SiNW@CNT at the maximum tensile deformation of 34.40% and 41.41% respectively.

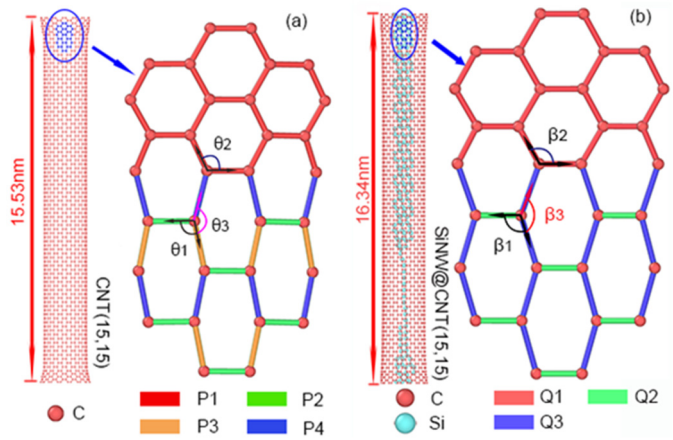

Figure 6. (a) Snapshot of CNT (15,15) at the maximum tensile deformation rate of 34.40%; (b) Snapshot of SiNW@CNT (15,15) at the maximum tensile deformation rate of 41.41%.

Further, bond angle distributions of the CNT and the SiNW@CNT at their maximum tensile deformation of 34.40% and 41.41% respectively are shown in Figure 5. The three major peaks of bond angle distributions can be identified at θ1=99.8°, θ2=120°, and θ3=159.1° respectively for the CNT shown in Figure 5(a), and ß1=102.8°, ß2=120°, and ß3= 153.7° respectively for the SiNW@CNT shown in Figure 5(b). By checking the structures in Figure 6, it is found that these angles correspond to different corners of the deformed hexagonal lattices, as marked in Figure 6. Here θ2 and ß2 remained constant, as they are located at the fixed end of the CNT and SiNW@CNT. On the other hand, θ1 was smaller than ß1 while θ3 was larger than ß3, showing that at tensile fracture, the deformation of the angles of the lattices for the CNT is larger than that of the SiNW@CNT.

3.3. Variation of bond length and bond angle in deformation

Since the analysis in the previous section demonstrates that the lattices of the two materials have different deformations at fracture, the change processes of their bond lengths and bond angles during the tensile deformation process were further analyzed.

Firstly Figure 7(a) shows the changes of the bond lengths with the increase of the strain. Note the four RDF peaks in Figure 4(a) are also distinctive in the RDF at other strain rates, therefore the bond lengths were read at the positions of these peaks at different strain rates. It can be seen that from ε=0 to ε=23.8%, P3 and P4 bond lengths increased linearly from 1.41 Å to 1.70 Å, and P2 slowly increased from 1.41 Å

to 1.45 Å. According to the strain rates, this stage coincided with the linear elastic deformation and yield deformation stages in Figure 2(a). When ε reached 29.8%, P3 and P4 underwent obvious splitting. As the deformation rate increased further, P4 length went up, P3 stayed the same, and P2 length increased linearly. When the tensile deformation of the CNT reached the maximum value of 34.0%, P2=1.56 Å, P3=1.74 Å, and P4=1.79 Å, On the other hand, the P1 length remained constant at 1.41 Å throughout the deformation process. This stage coincided with the strengthening stage in Figure 2(a).

On the other hand, the changes of the bond lengths of the SiNW@CNT with the strain rate are shown in Figure 7(b). Q3 increased linearly from 1.47 Å to 1.80 Å, and Q2 increased slightly from 1.47 Å to 1.48 Å at the tensile deformation rate of 0%-26.0%. Similarly, this stage also coincided with the linear elastic deformation and yield deformation stage in Figure 2(a). As the strain was increased to 41.2%, Q3 and Q2 slowly increased to 1.86 Å and 1.56 Å respectively. This stage was consistent with the strengthening stage in Figure 2(a). Q1 bond basically remained a constant of 1.47 Å throughout the stretching process. In general, when the CNT and SiNW@CNT are tensile fractured, the deformed lattice bonds of the SiNW@CNT are generally longer than those of the CNT, regardless of the radial bond length or axial bond length.

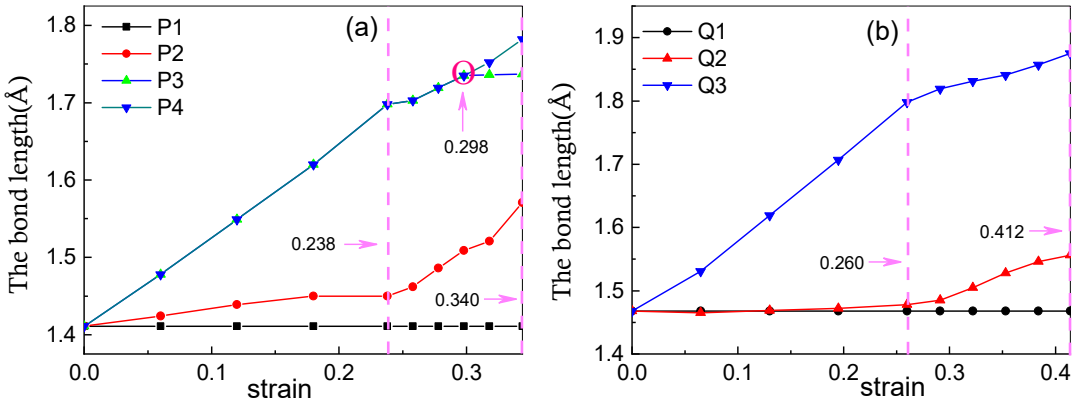

Figure 7. Variation of the C-C bond length in radial distribution function of CNT (a) and SiNW@CNT (b) during tensile deformation.

Besides the bond lengths, the changes of the bond angles of the CNT with the strain are shown in Figure 8(a). Similar critical changes can be found at the same strain rates. When the strain was increased from 0% to 23.8%, θ1 decreased slowly from 119 ° to 111 ° and θ3 increased from 120 ° to 138 °, corresponding to the linear elastic deformation and yield deformation stage in Figure 2(a). With the further increase of the strain from 23.8% to 34%, θ1 increased linearly to 100 ° and θ3 increased linearly to 160 °. And this stage was consistent with the strengthening stage in Figure 2(a). During the whole process, θ2 remained substantially constant, indicating that the fixed ends at both ends do not deform. Furthermore, the changes of the three main bond angles of the SiNW@CNT with the tensile deformation are shown in Figure 8(b). ß1 decreased from 119 ° to 117 ° and ß3 increased from 120 ° to 126 ° when the tensile deformation rate increased from 0 to 26.0%, which also aligns with the linear elastic deformation and yield deformation stage in Figure 2(a). When the strain continued to rise to 41.41%, ß1 increased to 103 ° and ß3 decreased to 154 °, both faster than the previous stage. Similarly, this stage is consistent with the strengthening stage in Figure 2(a). And ß2 basically remained constant throughout the stretch. The whole curve satisfies

$$4 * X1 + 2 * X3 \approx 6 * X2 = 720^{2}, (X = \theta, \beta), \quad (4)$$

which means that the influence of the curvature of the CNT on its bond angle can be neglected.

In the first two stages of tensile deformation, ie., the linear elastic deformation and yield deformation stages, the bond angle changes of the CNT and SiNW@CNT were relatively small. During the third stage of tensile deformation until the tensile fracture, the minimal bond angle decreased linearly, and θ1 of the CNT was closer to the right angle than ß1 of the SiNW@CNT. This result shows that the deformation angle of the CNT is larger than that of the SiNW@CNT during tensile deformation.

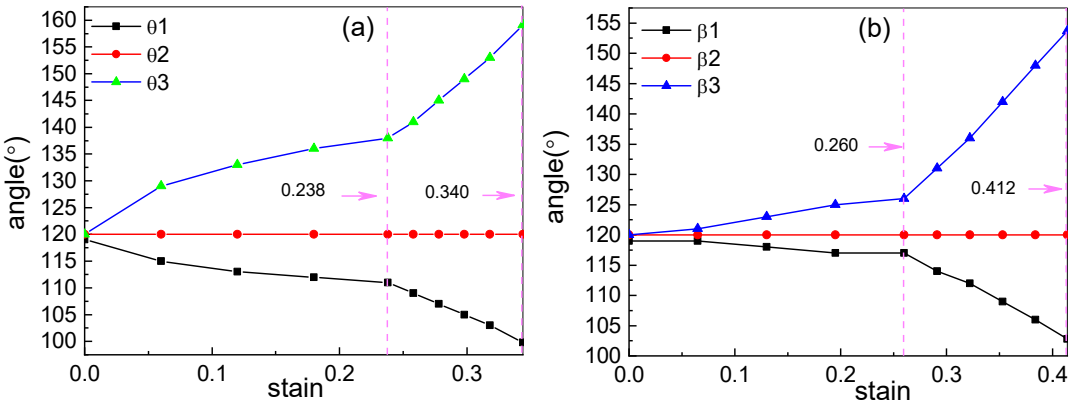

Figure 8. Three main bond angle distributions of CNT (a) and SiNW@CNT (b) during tensile deformation.

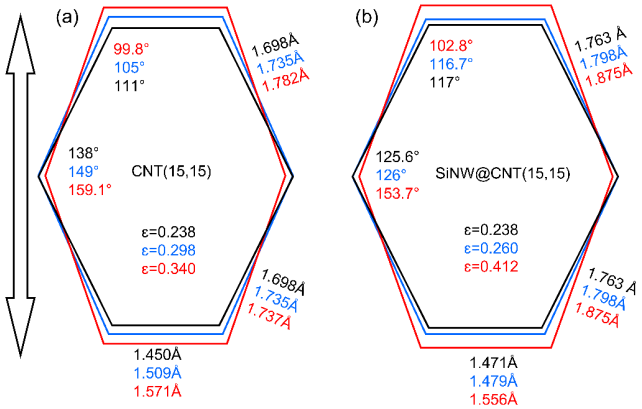

Figure 9. (a) Hexagonal lattice of the CNT at critical states ε=0.238, ε=0.298 and ε=0.340. (b) Hexagonal lattice of SiNW@CNT at critical states ε=0.238, ε=0.260 and ε=0.412.

Combining the changes in the bond lengths and angles, Figure 9 shows that the hexagonal lattices of the CNT at the critical states of ε=0.238, ε=0.298 and ε=0.340, and those of the SiNW@CNT at ε=0.238, ε=0.260 and ε=0.412. In these critical states, both the bond lengths and angles showed critical changes. It can be seen that generally the change of the hexagonal lattice was small, but it can have a great influence on its mechanical properties. However, the different changes in the two tubes in the strengthening stage are distinct. The lattices of the CNT had a larger deformation in this stage that those of the SiNW@CNT, particularly along the tensile direction.

3.4. Analysis of polygon defects

It was found that in tensile fracture in the literature that polygon defects emerge during the fracture of CNTs. That is, in some hexagonal lattices several C-C bonds will be broken and the related lattices change into defective polygons with edge numbers different from six, such as pentagons, heptagons, etc. Previous studies focused on the pentagon and heptagon defects [26], here we studied the polygon defects in a wider range by considering the defect polygons with edge numbers ranging from 3 to 10, and we traced the numbers of these polygons during the whole tensile deformation stage.

The numbers of polygon defects of the CNT and SiNW@CNT in the tensile deformation process are shown in Figure 10. As can be seen from Figure 10(a), when the tensile deformation rate reached 34.4% from 0%, the number of hexagons started to decrease sharply, while the numbers of triangles, quadrangles, pentagons and heptagons all started to increase. The number of triangles was the most, followed by pentagon defects and a small number of heptagon defects, indicating that lower-order ring defects were formed at this time. As the deformation continued to increases, the numbers of triangles, pentagons and

quadrangles decreased, while the numbers of higher-order rings with edge numbers greater than eight started to increase, which indicates that the lower-order ring defects may be dominant at the onset of fracture, but part of them can be gradually transformed into higher-order ring defects as fracture continues. Such changes in the defective polygons only occurred between the deformation rates of 34.4%-34.7%, and the whole fracture process took 7 ps.

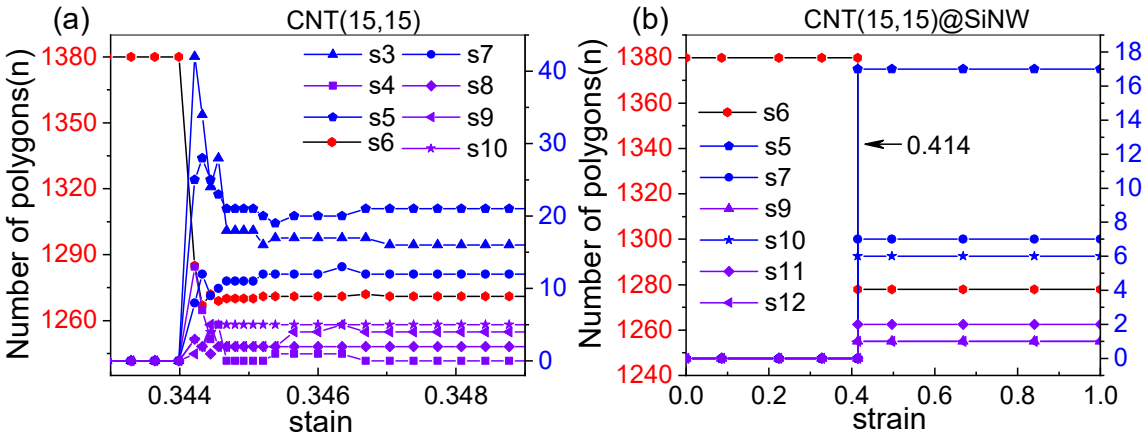

Figure 10. (a) The number of polygon defects of the CNT in the process of tensile deformation. (b) The number of polygon defects of SiNW@CNT in the process of tensile deformation. The hollow curve corresponds to the left Y-axis, and the solid curve corresponds to the right Y-axis.

On the other hand, Figure 10(b) shows that for the SiNW@CNT, when the deformation rate reached beyond 41.4%, the polygon defects were mainly pentagons, heptagons, and decagons, but the triangles were very few. This is because with the van der Waals force between the Si atoms and the C atoms strengthens the hexagon lattices, and hence the lattices are more difficult to have more than one edge broken and deform into triangles and quadrangles, so they mainly form pentagons and heptagons. The decagons can be formed by the breakage of the bond connecting the two hexagons, so they occupied a certain proportion. Correspondingly the fracture process was almost completed in only 0.5 ps, far shorter than that of the CNT. This is because the interaction between the inserted Si atoms and the C atoms makes the CNT less prone to necking [20].

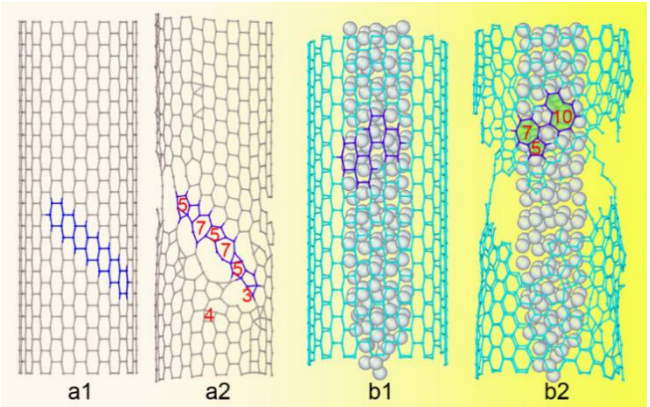

Figure 11. Snapshots for CNT (15,15) (a) and SiNW@CNT (15,15) (b) at two (1 and 2) typical tensile deformation.

The graphs before and after fracture were compared more intuitively in Figure 11. It can be seen that the triangle, pentagon and heptagon defects were linked into a long chain at the boundary of the fracture region. This is consistent with the results of experiments by R.S et al [27]. Although the SiNW@CNT

also has pentagon and heptagon defects after fracture, it is difficult to observe such long chains of defective polygons, as the defective polygons were more localized and scattered.

4. CONCLUSION

The tensile deformation processes of the CNT and SiNW@CNT have been comparatively studied by molecular dynamics simulation. Through the analysis and discussion of the simulated microstructure changes, the following conclusions can be drawn:

In the process of tensile deformation of the CNT and SiNW@CNT, the strain is mainly accommodated with the change of the bond length rather than that of the bond angle. Although the stress of SiNW@CNT is shared by the CNT and the SiNW, the yield of the SiNW during the strengthening stage results in the overall increase of the strain but the decrease of the stress.

At the maximum tensile deformation, the C-C bonds in the SiNW@CNT are longer and more uniformly deformed due to the van der Waals force between the SiNW and the CNT, which accounts for the change in the macroscopical tensile behavior.

After tensile fracture, the CNT mainly form long chains consisting of triangle, pentagon, and heptagonal defects, while SiNW@CNT cannot form long chains due to the lack of triangular defects. This is probably because the C-C bonds in the latter were strengthened by the encapsulated SiNW.

The results provide a better understanding on the microstructural changes of the CNT and its nanocomposites during tensile fracture, which has certain reference value for optimizing the mechanic properties of the CNT nanocomposites, and particularly for guiding the application of SiNW@CNT in engineering mechanics.

ACKNOWLEDGMENT

The work was supported by the National Natural Science Foundation of China (Grant No.61264004), and High-level Creative Talent Training Program in Guizhou Province of China (Grant No. [2015]4015).

REFERENCES

[1] S. Iijima, "Helical microtubules of graphitic carbon," Nature, vol. 354, no. 6348, pp. 56-58, 1991.
[2] L. C. Venema, A. G. Rinzler, R. E. Smalley, and C. Dekker, "Electronic Structure of Atomically Resolved Carbon Nanotubes," Nature, vol. 391, no. 6662, pp. 59-62, 1998.
[3] Ball and Philip, "Roll up for the revolution," Nature, vol. 414, no. 6860, pp. 142-144, 2001.
[4] Y. Zhang and M. Han, "Band gap of carbon nanotubes under combined uniaxial–torsional strain," Physica E: Low-dimensional Systems and Nanostructures, vol. 43, no. 10, pp. 1774-1778, 2011.
[5] J. Jyoti, S. Basu, B. P. Singh, and S. R. Dhakate, "Superior mechanical and electrical properties of multiwall carbon nanotube reinforced acrylonitrile butadiene styrene high performance composites," Composites Part B, vol. 83, pp. 58-65, 2015.
[6] K. Koziol et al., "High-Performance Carbon Nanotube Fiber," Science, vol. 318, no. 5858, pp. 1892-1895, 2007, doi: 10.1126/science.1147635.
[7] L. Wang, H. Zhang, Z. Zhang, Y. Zheng, and J. Wang, "Buckling behaviors of single-walled carbon nanotubes filled with metal atoms," Applied Physics Letters, vol. 91, no. 5, p. 051122, 2007.
[8] T. Belytschko, S. P. Xiao, G. C. Schatz, and R. S. Ruoff, "Atomistic simulations of nanotube fracture," Physical Review B, vol. 65, no. 23, p. 235430, 06/20/ 2002, doi: 10.1103/PhysRevB.65.235430.
[9] A. I. Hochbaum et al., "Enhanced thermoelectric performance of rough silicon nanowires," Nature, vol. 39, no. 14, pp. 163-167, 2008.
[10] L. Chen, J. L. Fan, and H. R. Gong, "Phase transition and mechanical properties of tungsten nanomaterials from molecular dynamic simulation," Journal of Nanoparticle Research, vol. 19, no. 3, p. 118, 2017.
[11] Tersoff and J., "Modeling solid-state chemistry: Interatomic potentials for multicomponent systems," Phys Rev B Condens Matter, vol. 39, no. 8, pp. 5566-5568, 1989.

[12] Jones and J. E., "On the Determination of Molecular Fields. I. From the Variation of the Viscosity of a Gas with Temperature," Proceedings of the Royal Society of London, vol. 106, no. 738, pp. 441-462, 1924.
[13] H. Liu, H. Zeng, T. Pan, W. Huang, and Y. Lin, "Pressure dependency of thermal boundary conductance of carbon nanotube/silicon interface: A molecular dynamics study," Journal of Applied Physics, vol. 112, no. 5, p. 053501, 2012.
[14] Q. Wang, K. M. Liew, and V. Varadan, "Molecular dynamics simulations of the torsional instability of carbon nanotubes filled with hydrogen or silicon atoms," Applied Physics Letters, vol. 92, no. 4, p. 043120, 2008.
[15] Melis Goktas et al., "Molecular mechanics of coiled coils loaded in the shear geometry," Chemical Science, vol. 9, no. 20, pp. 4610-4621, 2018.
[16] B. H. Zimm, "The scattering of light and the radial distribution function of high polymer solutions," The Journal of Chemical Physics, vol. 16, no. 12, pp. 1093-1099, 1948.
[17] D. H. Li, R. A. Moore, and S. Wang, "A computer and analytic study of the metallic liquid–glass transition. II. Structure and mean square displacements," Journal of Chemical Physics, vol. 89, no. 7, pp. 4309-4312, 1988.
[18] P. Lin, Z. He, S. Yuan, and J. Shen, "Tensile deformation behavior of Ti–22Al–25Nb alloy at elevated temperatures," Materials Science & Engineering A, vol. 556, no. 11, pp. 617-624, 2012.
[19] C. Pozrikidis, "Effect of the Stone–Wales defect on the structure and mechanical properties of single-wall carbon nanotubes in axial stretch and twist," Archive of Applied Mechanics, vol. 79, no. 2, pp. 113-123, 2009.
[20] C. Schoene and E. Scala, "Multiple necking phenomena in metal composites," Metallurgical Transactions, vol. 1, no. 12, pp. 3466-3469, 1970.
[21] D. Bozovic, M. Bockrath, J. H. Hafner, C. M. Lieber, H. Park, and M. Tinkham, "Plastic deformations in mechanically strained single-walled carbon nanotubes," Physical Review B, vol. 67, no. 3, p. 033407, 2003.
[22] Q. Zhao, J. R. Wood, and H. D. Wagner, "Stress fields around defects and fibers in a polymer using carbon nanotubes as sensors," Applied Physics Letters, vol. 78, no. 12, pp. 1748-1750, 2001.
[23] M. A. L. Marques, H. E. Troiani, M. Miki-Yoshida, M. Jose-Yacaman, and A. Rubio, "On the Breaking of Carbon Nanotubes under Tension," Nano Letters, vol. 4, no. 5, pp. 811-815, 2004.
[24] C. X. Fu, Y. F. Chen, and J. W. Jiao, "Molecular dynamics simulation of the test of single-walled carbon nanotubes under tensile loading," Science in China Series E Technological, vol. 50, no. 1, pp. 7-17, 2007.
[25] A. Stukowski, "Visualization and analysis of atomistic simulation data with OVITO-the Open Visualization Tool," Modelling Simul.mater.sci.eng, vol. 18, no. 6, pp. 2154-2162, 2010.
[26] M. Buongiorno Nardelli, B. I. Yakobson, and J. Bernholc, "Mechanism of strain release in carbon nanotubes," Physical Review B, vol. 57, no. 8, pp. R4277-R4280, 02/15/ 1998, doi: 10.1103/PhysRevB.57.R4277.
[27] R. S. Ruoff, D. Qian, and W. K. Liu, "Mechanical properties of carbon nanotubes: theoretical predictions and experimental measurements," Comptes Rendus Physique, vol. 4, no. 9, pp. 993-1008, 2003.